Creating sharp features by colliding shocks on uniformly irradiated surfaces

Miranda Holmes-Cerfon, Michael J. Aziz, and Michael P. Brenner
Harvard School of Engineering and Applied Sciences and Kavli Institute for Bionano Science and Technology, 29 Oxford Street, Cambridge, Massachusetts 02138, USA

(Received 24 October 2011; revised manuscript received 6 April 2012; published 24 April 2012)

Using a theoretical analysis of the ion beam sputtering dynamics, we demonstrate how ion bombardment on an initially sloped surface can create knife-edge-like ridges on the surface. These ridges arise as nonclassical shocklike solutions that are undercompressive on both sides and appear to control the dynamics over a large range of initial conditions. The slope of the ridges is selected uniquely by the dynamics and can be up to 30 or more depending on the orientation dependence of the sputtering yield. For 1 keV Ar^+ on Si(001), the scale of the ridge is $\approx$2 nm. This is much smaller than the most unstable length scale and suggests a method for creating very steep, very sharp features on a surface spontaneously, by prepatterning the surface to contain relatively modest slopes on the macroscale.

DOI: 10.1103/PhysRevB.85.165441 PACS number(s): 79.20.Rf, 43.25.Cb, 43.40.Jc, 81.16.Dn

I. INTRODUCTION

Fabricating nanoscale features on a surface is increasingly important, but many methods suffer throughput limitations too restrictive to permit them to be widely implemented on a large scale. It is therefore of interest to find techniques stemming from self-organization principles, whereby macroscale features dynamically give rise to complex small-scale structures.[1] A promising method is ion bombardment.[2–4] This erodes a surface at different rates depending on the slope of the surface, so intricate two-dimensional structures can emerge. Currently focused ion beam bombardment is used to micromachine tall, steep features[5,6] and to sculpt nanopore single-biomolecule detectors,[7,8] while uniform ion bombardment of a flat surface is used to create semiconductor quantum dots from the linear instabilities that are excited.[9–11] The utility of these techniques is, however, limited. Focused ion beams are costly in both time and energy, while uniform irradiation of a flat surface cannot achieve very steep nor very sharp structures because of saturation and wave-number constraints on the linearly unstable modes.

Here we predict that it is possible to create very sharp, steep features from uniform ion bombardment, by starting with a surface that is prepatterned to have modest slopes on the macroscale. This allows the dynamics to become nonlinear, without imposing a large cost: Such a prepatterning is relatively cheap to achieve, for example, using optical standing waves. If the initial slopes are larger than a critical value, the surface spontaneously develops much larger slopes under uniform ion bombardment (see Fig. 1). Specifically we show that it evolves to a knife-edge-like ridge, whose shape is a fixed function of the material, ions, and energy but is independent of the initial patterning. One could imagine creating a large-scale pattern with these robust nanoscale ridges to obtain a material that is currently too costly to probe experimentally.

The knife-edge ridge is a particular nonclassical traveling wave solution to the governing equations, and to understand why and when it arises we must investigate the full landscape of traveling wave solutions. We proceed as follows. In Sec. II we introduce the governing equations and review the definitions of classical and nonclassical traveling wave solutions. In Sec. III we compute the entire set of traveling wave solutions for a given material and energy, show that it supports an isolated steep, sharp, nonclassical solution that looks like a knife edge, and discuss how this generalizes for arbitrary materials. Section IV investigates the dynamics of the height evolution and how these can be understood from the set of traveling wave solutions; in particular we show that a wide range of conditions leads to the knife-edge solution. Section V shows how the knife-edge solutions vary with different materials and energies, and Sec. VI discusses the effect of an approximation we make to simplify the analysis. Finally, we offer concluding remarks in Sec. VII.

II. GOVERNING EQUATIONS AND TRAVELING WAVE SOLUTIONS

Our analysis begins with the classical macroscopic description to ion beam sputtering,[2] in which the height $h(x,t)$ of the surface is described by a nonlinear partial differential equation, representing the combined effects of atom sputtering, atom redeposition, and additional smoothing physics such as surface diffusion or ion-enhanced viscous flow. We consider surface morphologies that vary in one direction only. When the radius of curvature of the surface is much larger than the lateral scale over which an ion deposits its kinetic energy, the height evolves according to[12]

$$h_t + Y(|\nabla h|) = D(|\nabla h|)h_{xx} + B_0\sqrt{1+b^2}\frac{\partial^2\kappa}{\partial s^2}. \quad (1)$$

Here $Y(b)$ is the yield function, which gives the average velocity of erosion of the surface as a function of its slope $b = |\nabla h|$ (or equivalently the angle of the incoming ion beam), $D(b)$ describes the second-order effects of sputtering and redistribution, κ is the surface curvature, and $\frac{\partial}{\partial s} = \frac{1}{\sqrt{1+b^2}}\frac{\partial}{\partial x}$ is the arc-length derivative. The final term represents surface diffusion or viscous flow confined to a thin surface layer, and the factor $\sqrt{1+b^2}$ accounts for the evolution of the height in the direction parallel to the incoming ions.

Since we are interested in dynamical regimes producing the smallest scale structures, we consider the limit where the dominant smoothing mechanism is fourth order, so the $D(b)$ term is negligible in comparison. This simplifies the analysis

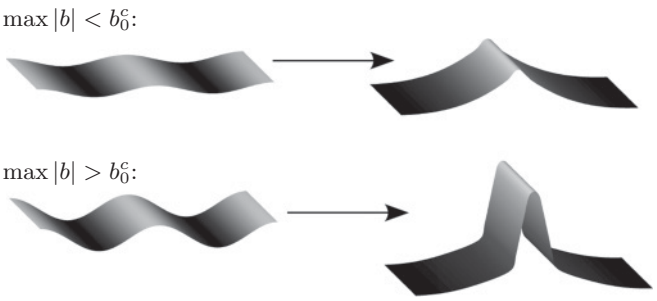

FIG. 1. Schematic of surface height evolution. When the maximum slope of the initial patterning (left) is less than a critical value (top), there is little slope amplification. When the slope of the initial patterning is greater than a critical value (bottom), the slope is amplified considerably and the knife-edge ridge forms.

and allows us to consider a smaller range of parameters; in addition this term is not well constrained by measurements, so it is difficult to incorporate quantitatively in a theoretical paper at the present time. The validity of this approximation is likely ion energy dependent, and we discuss it further in Sec. VI.

To analyze Eq. (1), it is convenient to use the slope $b = h_x$ as the dynamical variable. After nondimensionalizing lengths by $L = (B_0/Y_0)^{1/3}$, times by $T = L/Y_0$, and the yield function as $\tilde{Y}(b) = Y(b)/Y_0$ where $Y_0 = Y(0)$, we obtain

$$b_t + \tilde{Y}(b)_x = -\frac{\partial^2}{\partial x^2}\left\{\frac{1}{\sqrt{1+b^2}}\frac{\partial}{\partial x}\left[\frac{b_x}{(1+b^2)^{3/2}}\right]\right\}. \quad (2)$$

The left-hand side has the mathematical structure of a nonlinear conservation law, which arises in many physical contexts and typically results in nonlinear waves such as shocks or rarefaction waves.[13] The local advection velocity is given by $\tilde{Y}'(b)$, which varies with b and so causes the slopes to steepen; this effect is counteracted by fourth-order smoothing. This steepening can lead to a sharp jump between some slope b_l on the left and some slope b_r on the right, which can propagate as a traveling wave.

Our numerical simulations (described below) indicate that such traveling wave solutions control the long-time dynamics of (2) and provide an organizing principle for discovering initial surface shapes leading to knife-edge solutions. It is therefore useful to start our study by characterizing the pairs (b_l,b_r) between which such traveling solutions can exist. We seek solutions to (2) of the form $S(\eta) = S(x - ct)$ with boundary conditions $S(-\infty) = b_l$, $S(\infty) = b_r$, $S'(\pm\infty) = 0$. After integrating from $+\infty \to \eta$, we obtain a third-order boundary value problem for the traveling wave:

$$c(S - b_r) - [Y(S) - Y(b_r)] = B_0\left\{\frac{1}{\sqrt{1+S^2}}\left[\frac{S'}{(1+S^2)^{3/2}}\right]'\right\}', \quad (3)$$

with boundary conditions $(S,S',S'')|_{-\infty} = (b_l,0,0)$, $(S,S',S'')|_{\infty} = (b_r,0,0)$. The speed c is determined by integrating (2) from $-\infty$ to $+\infty$ to give

$$c = \frac{Y(b_r) - Y(b_l)}{b_r - b_l}. \quad (4)$$

Strikingly not all pairs (b_l,b_r) can admit a traveling wave solution. The reason for this can be heuristically understood by a dimension-counting argument. A traveling wave solution is a trajectory $(S(\eta),S'(\eta),S''(\eta))$ in three-dimensional space, connecting the left-hand endpoint $(b_l,0,0)$ to the right-hand endpoint $(b_r,0,0)$. For a solution to exist, the set of paths leaving the left-hand point [the unstable manifold, denoted $\mathcal{US}(-\infty)$] must intersect the set of paths which enter the right-hand point [the stable manifold, denoted $\mathcal{S}(\infty)$], and the intersection set must be at least one-dimensional. Whether or not this can happen depends on the dimensions of $\mathcal{US}(-\infty)$, $\mathcal{S}(\infty)$. These are calculated by linearizing the ODE obtained from (2) about each of the boundary points at $\pm\infty$, and looking for exponentially growing modes $\propto e^{\lambda\eta}$. We find that $\lambda^3 \propto c - Y(b_{l(r)})$, so $\mathcal{US}(-\infty)$ is two-dimensional when $c < Y(b_l)$ and one-dimensional otherwise, and $\mathcal{S}(\infty)$ is two-dimensional when $c > Y(b_r)$ and one-dimensional otherwise.

There are three possible families of solutions. When both $\mathcal{US}(-\infty)$, $\mathcal{S}(\infty)$ are two-dimensional, a solution is the intersection of two surfaces in $\mathbb{R}^3$; this can lead to an intersection curve. Solutions of this type are classical shocks and satisfy the Lax entropy condition $\tilde{Y}'(b_l) > c > \tilde{Y}'(b_r)$, so that the solution behind the jump moves faster than it and the solution in front of the jump moves more slowly: The shock is compressed from both sides.

When either $\mathcal{US}(-\infty)$ or $\mathcal{S}(\infty)$ is one-dimensional, a solution exists when a curve and a surface intersect in such a way that the intersection contains a curve; this is almost always impossible. However, if we introduce another parameter, such as by varying b_l or b_r, then this extra dimension means it may become possible to find a solution. This will violate one of the inequalities in the Lax entropy condition; hence such solutions are typically called *undercompressive*.[14,15] Because we must vary a parameter to find a solution, the set of values which admit undercompressive solutions are a curve in (b_l,b_r) space.

The final possibility is that both $\mathcal{US}(-\infty)$ and $\mathcal{S}(\infty)$ are one-dimensional, so we must vary two parameters to find a solution. Such solutions will be undercompressive from both sides, so we call them *doubly undercompressive*, and they will be isolated points in (b_l,b_r) space.

III. TRAVELING WAVE LANDSCAPE

We numerically search for the values of (b_l,b_r) which admit traveling wave solutions (see Sec. A 1 for methods), using as a model the yield function for 1 keV Ar^+ ion bombarded Si(001). In nondimensional form this is given by

$$\frac{Y(\theta)}{Y(0)} = (\cos\theta)^{-f}\exp\{-\Sigma[(\cos\theta)^{-1} - 1]\}, \quad (5)$$

where[16] $\cos\theta = (\sqrt{1+b^2})^{-1}$, $\Sigma = f\cos\theta_{\text{opt}}$, $f = 2.36$, and $\theta_{\text{opt}} = 69.5$ (see Fig. 2). Figure 3 plots the solutions we have found for $|b_l|,|b_r| \leqslant 8$. There are five two-dimensional regions of compressive solutions (red patches), four curves of undercompressive solutions (red lines), and exactly one doubly undercompressive solution (red star). Because there is symmetry in the traveling wave equation under time and space reversal, this figure is symmetric about the line $b_l = -b_r$.

The doubly undercompressive solution, at $(b_l,b_r) = (b_*, -b_*)$ where $b_* = 4.7$, corresponds to a sharp change in slope which is antisymmetric about 0 (Fig. 3, right), so the height of the surface looks like a knife edge. The change happens

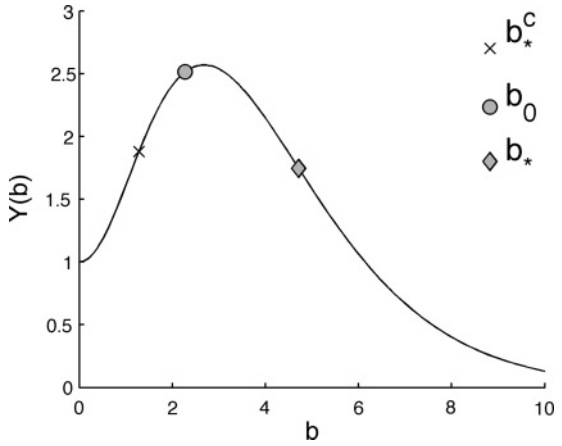

FIG. 2. Yield function (5) used as a case study. Markers indicate undercompressive shock b_0, doubly undercompressive shock b_*, and the smallest slope b_*^c above which b_* emerges.

over a distance $x' = 3.7$, so the radius of curvature at the tip is $M^{-1} = 2.5^{-1}$. Madi *et al.*[16] estimate $B_0 = 0.062$ nm^4/s and $Y_0 = 3.7 \times 10^{-4}$ nm/s, which implies a dimensional radius of curvature of $L/M = (B_0/Y_0)^{1/3}/2.5 = 2.2$ nm. This is several times smaller than the most unstable wavelength of 9.8 nm. Experimental realization of this solution would therefore provide a novel method to create very small-scale, sharp features.

We should note that the approximation (1) breaks down when the radius of curvature of the surface becomes equal to the length scale over which an ion deposits its energy. This length scale is at a maximum of 1.6 nm for a flat surface, decreasing to 0.55 nm for a surface with slope b_*.[12,16] As these scales are approaching the radius of curvature of the doubly undercompressive solution, additional physics may be required to quantitatively describe the dynamics after it has formed.

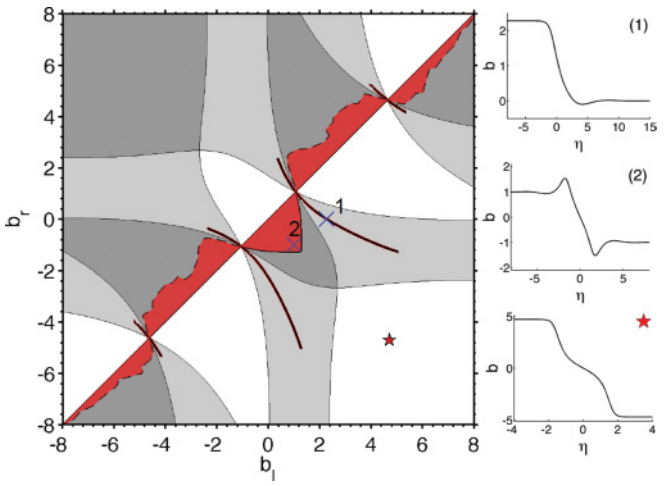

FIG. 3. (Color online) Red shading (darkest), red lines, red star: Boundary conditions (b_l,b_r) yielding traveling wave solutions to (2). Background shading indicates the type of solution possible: compressive (dark), undercompressive (medium), doubly undercompressive (white). Dashed line on boundary of some red regions indicates uncertainty in exact location of boundary. Selected solutions (for slope $b = h_x$) with given boundary conditions: top $(b_0, 0)$, middle $(1, -1)$, bottom $(b_*, -b_*)$.

The traveling wave landscape will change with the yield function, which varies with the substrate, ions, and energy. We have investigated a variety of experimentally measured yield functions and found that the qualitative features of the traveling wave landscape, such as possessing a single doubly undercompressive solution, are similar to Fig. 3, but that quantitative features, such as the slope of the solution, will change. Therefore we focus on the above yield function as a model to carry out our investigation and comment on how it will vary for other materials in Sec. V.

IV. NUMERICAL SOLUTIONS TO THE GOVERNING EQUATIONS

We have investigated ways of forming this knife-edge solution by solving the PDE (2) numerically, searching for initial conditions where the system spontaneously evolves to the knife edge. (See Sec. A for a description of our numerical procedure.) We will compare our results to the traveling wave solutions found in Sec. III. Because these solutions become shocks in the limit $B_0 \to 0$, we use the words "shock" and "solution" interchangeably.

A. Fixed-slope boundary conditions

We first consider initial conditions in which the slopes at the edges are constant. Our simulations demonstrate that if the slopes at the edges are fixed to values in a red region for which there exists a compressive shock, the solution evolves to the corresponding traveling wave.

If we start with boundary values for which there is *not* a traveling wave, then the solution in intermediate regions creates at least two shocks, at least one of which will be undercompressive. For example, if we start with the pair $(b_l,b_r) = (1.6,0)$ for which there is no compressive shock, the solution after a long time forms a compressive shock (1.6,2.3) and an undercompressive shock (2.3,0). Both move rightwards, but the compressive shock moves more slowly, so the region of high slope $b = 2.3$ gets larger with time; see Fig. 4 (left).

This particular undercompressive shock (which we call $b_0 = 2.3$), connecting an undetermined value b_l on the left to a flat surface $b_r = 0$ on the right, is important because it arises spontaneously whenever a surface is initially patterned to have a compact region with large enough slopes, surrounded by a flat surface. We have determined via traveling wave solutions that the maximum value of b_l for which there is a compressive wave connecting it to $b_r = 0$ is

$$b_0^c = 1.257, \tag{6}$$

and we have found numerically that it arises whenever $b_l > b_0^c$. It was first pointed out theoretically in Chen *et al.*,[12] who also observed it experimentally in 30 keV gallium on silicon. The pair $(b_0,0)$ is marked with a blue cross in Fig. 3, and the particular solution shown in the sidebar.

A similar behavior occurs for other pairs; for example $(b_l,b_r) = (3,-1)$ evolves to a compressive shock (3,4.3) moving leftwards and an undercompressive shock (4.3,−1)

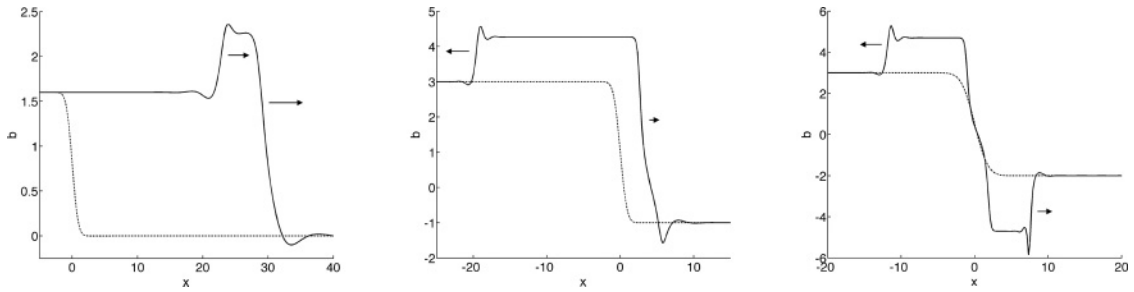

FIG. 4. Solutions to the PDE (2) for different boundary conditions. Left: $b_l = 1.6, b_r = 0$. Middle: $b_l = 3, b_r = -1$. Right: $b_l = 3, b_r = -2$. Initial condition indicated as a dotted line, solution $b(x)$ after a long time is a solid line. The relative speeds of the steep features of each solution are indicated by the relative sizes of the adjacent arrows.

moving rightwards. In height coordinates this is an asymmetric ridge moving to the right. See Fig. 4 (middle).

Qualitatively different behavior occurs for a pair such as $(3,-2)$. In this case the dynamics selects a combination of three shocks: in the middle is the doubly undercompressive shock $(4.7,-4.7)$, which has speed $c = 0$, and traveling away on either side are compressive shocks $(3,4.7)$ and $(-4.7, -2)$. The surface evolves to a stationary knife edge that gets taller with time. This three-wave structure with the doubly undercompressive shock in the middle is very robust; a wide range of boundary conditions give rise to it.

B. Calculus of traveling wave solutions

The above investigation suggests a form of calculus can be applied to Fig. 3 to determine the long-time solution to the PDE selected by a given pair of boundary values (b_l, b_r).

Let us return to the point $(b_l, b_r) = (1.6,0)$. This is in a dark-gray region of Fig. 3, where there is no traveling wave solution, so it must evolve to intermediate values $Y_1, Y_2, \ldots$ to form several shocks as $(1.6, Y_1)$, (Y_1, Y_2), $(Y_2, 0)$. To determine the possible values of Y_1, Y_2 we do the following. Put three hypothetical shocks on the figure at $X_1 = (1.6,0)$, $X_0 = (1.6,1.6)$, $X_2 = (0,0)$. Figure 5 shows this construction. The shocks from left to right connect as X_0, X_1, X_2. Now, we want to move the points to put each of them in a red region, but in such a way that they still represent a sequence of shocks: The second value of X_i equals the first value of X_{i+1}, and the first value of X_0 and second value of X_2 are fixed to satisfy the boundary conditions. The points can move as follows: If X_1 moves up (down), then X_0 moves left (right) by an equal amount, and if X_1 moves right (left), then X_2 moves up (down) by an equal amount.

It can be seen by examination that the only way that X_1 can move to keep X_0, X_2 in a red region is right or up, and that X_1 must lie on the nearest curve of undercompressive solutions. It can lie anywhere on the curve from $(1.6,0.7)$ to $(2.3,0)$ and still keep X_0, X_2 in a red region. So why does it choose the extreme point, where $X_0 = (1.6,2.3)$, $X_2 = (0,0)$?

To answer this consider the speeds of the resulting shocks. Because the undercompressive shocks contained on the curve in question are compressive from the right, characteristics enter the shock from this direction, so any nonconstant solution to the right of X_1 will eventually be subsumed by it. Therefore X_2 must lie on the diagonal. Indeed, computing the speeds for the other extreme point, $X_1 = (1.6,0.7)$, $X_0 = (1.6,1.6)$, $X_2 = (0.7,0)$, shows that $c(X_1) = 0.9$ and $c(X_2) = 0.5$ [see Eq. (4)], so X_1 will catch up to X_2 and the latter cannot exist as a long-time solution.

We have found this behavior generically follows through for the points to the left of the curve of undercompressive solutions in the lower right-hand quadrant. However, for boundary values below the minimum of the curve, such as the point $(3,-2)$, there are no longer feasible solutions for X_1 on the undercompressive curve. In this case X_1 moves to the doubly undercompressive solution $(4.7,-4.7)$. Because this is undercompressive from both sides, characteristics move away from it on either side so there can be two shocks surrounding it: $X_0 = (3,4.7)$, $X_2 = (-4.7,-2)$.

It can be seen by examining Fig. 3 that the the doubly undercompressive solution arises for a large set of boundary conditions, a finding that is consistent with our numerical experiments.

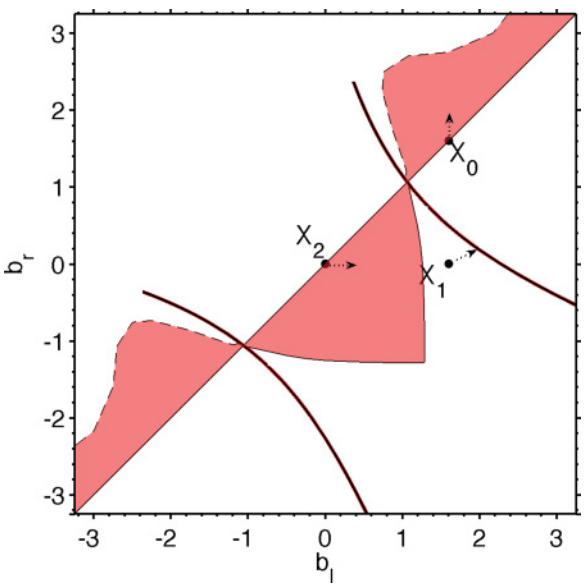

FIG. 5. (Color online) Constructing a triplet of feasible shocks (X_0, X_1, X_2) which move so they all lie in a red region, corresponding to a pair of boundary conditions yielding traveling wave solutions to (2).

C. Dynamically creating the doubly undercompressive solution

The fact that the knife edge arises for a large set of boundary conditions suggests a method for creating sharp features experimentally: by patterning the surface initially to contain slopes that steepen to the doubly undercompressive solution. We expect this solution to arise when the magnitude of the initial slope is large enough, as shown in Fig. 1. In this section we determine a criterion on the initial slope that guarantees the doubly undercompressive solution will emerge for fixed boundary conditions, and then we demonstrate numerically that the dynamically evolving case can be partially understood using the solutions for fixed boundary conditions.

To determine a lower bound on the initial slope, we first consider a simplified problem that is antisymmetric about $x = 0$, with fixed boundary conditions $b_l = -b_r$. By computing traveling wave solutions along the diagonal $b_l = -b_r$ in Fig. 3, we determine that the maximum compressive shock occurs at $b_l = b_*^c$, where

$$b_*^c = 1.28. \tag{7}$$

Next, we solve the governing PDE numerically using an initial condition containing two equal but oppositely sloped regions separated by a flat region in between: We can think of this as identical shocks moving in opposite directions that collide. As predicted by analysis in Secs. IV A and IV B, these initial conditions lead to a compressive shock when $b_l < b_*^c$, but to the doubly undercompressive shock plus two compressive shocks when $b_l > b_*^c$. Figure 6 shows the time evolution of one initial condition when $b < b_*^c$, and two initial conditions with different slopes when $b > b_*^c$; both of these conditions approach the same doubly undercompressive solution.

What is striking about this is that it provides an *amplification* of the slope of the surface, to a universal value that depends only on the surface properties. This phenomenon is the major discovery of this paper.

An argument can be made that, at least transiently, one need consider only the symmetric case, and in doing so we relax the criterion on the initial slope even further. When the sloped regions are initially far apart, they effectively see a flat surface ahead, so given sufficient initial slopes, they develop the undercompressive shock b_0 at their leading edges. When these shocks meet, they initially follow the dynamics appropriate to shocks of slope b_0 that collide. Since $b_0 > b_*^c$, this automatically develops into the doubly undercompressive shock.

Therefore, we predict that the doubly undercompressive shock will emerge dynamically when

$$\max\{\text{initial magnitude of slope}\} > b_0^c \tag{8}$$

(on each side), provided

$$b_0 > b_*^c, \tag{9}$$

where b_0^c was the minimum value required to develop the undercompressive shock. Condition (9) is a feature of the traveling wave landscape that depends on the yield function. We have found it to hold for all the functions of Yamamura type that we have investigated (see Sec. V). However, it need not be true for general yield functions or smoothing terms: As a side investigation we have solved the traveling wave problem with a linearized fourth-order term $-B_0\Delta\Delta b$ and found that only certain yield functions satisfy the inequality. Therefore curvature-dependent evolution is critical to achieving steep features.

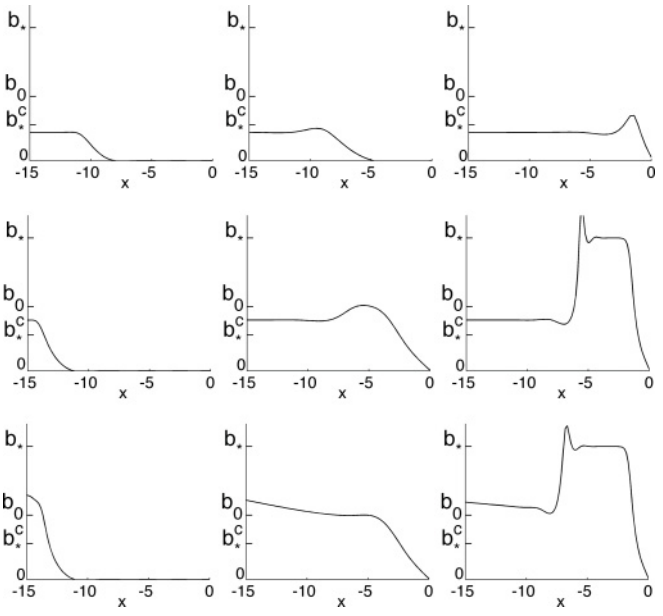

FIG. 6. Time evolution of antisymmetric initial conditions, with boundary slopes held fixed at $(b_l, -b_l)$. Time advances from left to right. Top: Boundary condition $b_l = 1 < b_*^c$. Two compressive shocks form and approach each other. When they collide, they form a compressive shock that does not change with time. Compare with solution (2) in Fig. 3. Middle: Boundary condition $b_l = 1.8 > b_*^c$. Two undercompressive shocks form and approach each other (each is trailed by a compressive shock). When they collide, they form the doubly undercompressive shock and two compressive shocks that travel away. Bottom: Boundary condition $b_l = 3 > b_*^c$. This also forms two undercompressive shocks that collide and form the same doubly undercompressive shock. Only half of each simulation is shown as the curves are antisymmetric about $x = 0$.

We next demonstrate that the doubly undercompressive shock can arise dynamically, without fixing the boundary conditions but by prepatterning the surface. We have found that criterion (8) applied to the initial patterning is sufficient to create the doubly undercompressive shock dynamically, although the length of time for which it exists will depend on other features of the initial condition such as the length and initial separation of the sloped regions. Figure 7 shows the dynamics for one possible experimental setup. The initial surface is a wide ridge, whose sides have slopes ± 3, tapering to a flat surface at the edges of the domain. Initially the sides move toward each other, creating the undercompressive shock from $\pm b_0$ to 0 at their leading edges. When they approach there is a sharp jump in slope from $+b_0$ to $-b_0$. Since $b_0 > b_*^c$, the system evolves to the doubly undercompressive shock: The slopes at the jump steepen to $\pm b_*$, forming a steep, knife-edge shape, while the location of the jump does not change. When the whole ridge has moved in the knife edge decays rapidly to zero. It is notable that the doubly undercompressive shock

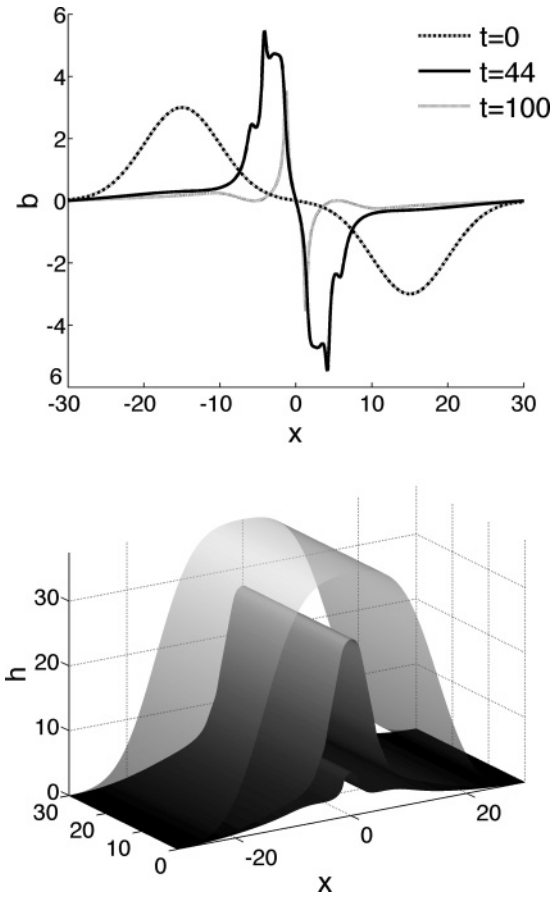

FIG. 7. Dynamics of colliding steep features at initial, intermediate, and near-final times. Top: slope, bottom: height.

evolves quickly enough to exist stably over a period of time despite the dynamically evolving conditions.

A schematic of the height evolution of a prepatterned surface illustrating criterion (8) is shown in Fig. 1.

V. OTHER MATERIALS

Thus far we have computed features of the traveling wave landscape, such as b_*, b_0, b_0^c, and b_*^c, for a single yield function. However, the traveling wave landscape will change with the yield function, which varies with the substrate, ions, and energy. We have solved for selected features of the landscape numerically for the family of yield functions compiled by Yamamura,[17] who showed that many experimentally measured yield functions can be represented using (5) and fitting for f, θ_{opt}.

As we vary these parameters within experimentally observed bounds, the qualitative features of Fig. 3 are similar to the case study, but the numbers change. They are most sensitive to θ_{opt}, varying only a little with f. To illustrate the range of variation, Fig. 8 plots the slope b_* of the doubly undercompressive solution and its nondimensional radius of curvature M versus θ_{opt} at $f = 2$, and shows that the steepest, sharpest features occur at the largest values of θ_{opt}. For example, 4 keV H on Ni has $\theta_{\text{opt}} = 84.2^\circ$, where the slopes are predicted to be $b_* = 29$.

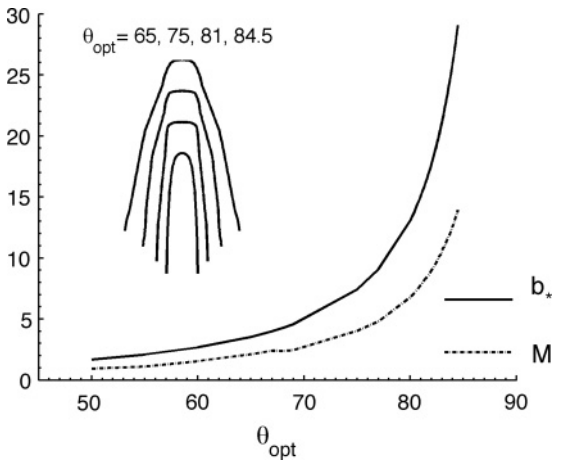

FIG. 8. Solid line: Slope b_* of the doubly undercompressive solution for yield functions of form (5), with $f = 2$. Dashed line: Coefficient M determining radius of curvature $(B_0/Y_0)^{1/3}/M$ of this solution. Inset: Selected doubly undercompressive solutions in height variable.

This opens up an interesting possibility: to choose or to engineer a yield function specifically to obtain the desired radius of curvature. Changing the material in this way opens the window for making very sharp structures.

VI. SECOND-ORDER TERM $D(b)$

Our analysis above hinges on the assumption that the second-order term can be neglected. This is a valid approximation to make when the dynamics select either scales small enough that the fourth-order term dominates or slopes large enough that $D(b)$ is small, but in actual experiments this may or may not be the case. Here we briefly consider the effect of adding a second-order term.

We include second-order effects in (2) by adding a term of the form $\delta\tilde{D}(b)b_{xx}$, where $\delta = \frac{D(0)}{LY_0} = \frac{D(0)}{B_0^{1/3}Y_0^{2/3}}$ is a nondimensional parameter governing the size of this term for a flat surface, and $\tilde{D}(b) = D(b)/D(0)$. We first solve for features of the traveling wave problem with constant second-order diffusivity, $\tilde{D}(b) = \delta$. As δ increases, b_*^c,b_0^c increase and b_0, b_* decrease, until eventually they collide and the nonclassical shocks no longer exist. This is consistent with results for a fourth-order thin film model.[15]

In a more realistic model, we have solved the PDE (2) numerically with a second-order term obtained from experiments in Madi *et al.*,[16] whose dimensionless form is

$$D(b) = \delta\frac{1-b^2}{1+b^2}\exp[-\Sigma(\sqrt{1+b^2}-1)]. \qquad (10)$$

The numerically observed value of b_* changes extraordinarily little with δ, by less than 1%. Presumably this is because $D(b) \ll D(0)$ when b is large, which is the situation of interest. However, b_*^c increases with δ and $b_*^c > b_0$ when $\delta \gtrapprox 0.5$, so that colliding two undercompressive shocks no longer leads to the doubly undercompressive shock. As δ increases the dynamics become increasingly turbulent, and for $\delta \gtrapprox 1$ we

have not found evidence of the doubly undercompressive shock.

We have not attempted to estimate δ for given materials because the field is in a bit of a paradoxical situation with respect to the size of this term in the parameter regime in question. On one hand, Chen *et al.*[12] observed that at 30 keV gallium on silicon, there were undercompressive shocks, which can happen only when δ is small. At the time that paper was written, it was believed that the second-order term was caused by a Sigmund-like sputter erosion-based mechanism. In the intervening time, Norris *et al.*[18] and Madi *et al.*[16] have demonstrated that for 1 keV argon on silicon, the dominant roughening and smoothing mechanism is from the ion impact-induced redistribution of those atoms which are *not* sputtered away, for which there is currently no first principles theory. Because of this, quantifying $D(b)$ for various systems and understanding how it changes with various parameters is still in process,[16,18–21] so we are unable to make specific recommendations about when the approximation $\delta \ll 1$ is valid.

We do, however, note that Chen[22] contains images showing that sharp, razor-blade-like structures can emerge on magnesium sputtered with 30 keV gallium when prefabricated pits expand and collide. Combined with the fact that undercompressive shocks were observed experimentally in Chen *et al.*,[12] this makes us optimistic that the doubly undercompressive shock will also be demonstrated experimentally. A simple test would be to start with a shallow ridge and see if it steepens to a sharper ridge; if it does, then the doubly undercompressive shock can serve as an organizing principle for explaining self-steepening mechanisms on surfaces.

VII. CONCLUSIONS

We have shown that there is a wide class of initial conditions that cause an ion sputtered surface to evolve to a knife-edge-like shape, with very steep slopes and a radius of curvature much smaller than the minimum wavelength of the instability leading to sputter rippling. Our analysis hinges on the existence of traveling wave solutions to the governing nonlinear partial differential equation, and the fact that when the smoothening mechanism is fourth order (arising, for example, from surface diffusion or surface-confined viscous flow) these solutions are a discrete set. The knife-edge-like solution occurs as an isolated point in the space of boundary conditions and arises from initial slopes that are larger in magnitude than a material-dependent number b_0^c. Because the slopes of the knife edge are $b_* \gg b_0^c$, the initial slopes can be amplified considerably by the dynamics.

These calculations suggest an entirely new arena for creating self-organized nanometer-scale structures with an ion beam: by prepatterning a surface so it evolves to structures with steep, sharp features when ion sputtered under appropriate conditions. Our calculations predict that one can achieve arbitrarily steep, sharp structures by choosing the materials and energies appropriately.

Although our analysis was restricted to structures that vary in only a single dimension, we expect it will be possible to extend this to two-dimensional structures. Ultimately, one would like to answer the inverse problem: Find a range of prepatterned surface shapes that evolve to a given design under uniform irradiation.

ACKNOWLEDGMENTS

We gratefully acknowledge support from the National Science Foundation through DMS-0907985, the Kavli Institute for Bionanoscience and Technology, and the Harvard MRSEC.

APPENDIX

1. Numerical procedure for traveling wave solutions

Traveling wave solutions to (2) were computed using a collocation method, as implemented by the function bvp4c provided by Matlab. This takes an initial guess for the solution and the grid it is defined on, and iteratively solves a set of nonlinear algebraic equations to better approximate the true solution on an updated grid, with boundary conditions.[23,24] If this produces a convergent result, whose residual is smaller than a desired tolerance level, we consider a solution to exist for that particular choice of b_l,b_r. The method also allows us to consider boundary values which vary by including them as extra variables in the problem. This lets us look for undercompressive solutions and gives us the particular values of b_l,b_r as part of the solution. In implementing the method we choose the length of the interval to be 80 nondimensional units. To improve the likelihood of finding a solution we use a continuation procedure, starting with a pair (b_l,b_r) for which solution is easy to obtain, and using this to produce an initial guess for a pair (b_l',b_r') slightly perturbed from the original.

To find a doubly undercompressive solution, we restrict to solutions that are antisymmetric about 0 and solve (3) on $(-\infty,0)$ with right-hand boundary condition $S(0) = 0, S''(0) = 0$. By allowing the left-hand value b_l to vary we obtain a single solution $b_l = b_*$.

Boundaries of regions where solutions exist are estimated by fixing b_r at increments of 0.25 and using continuation on b_l. When incrementing b_l by an amount smaller than the tolerance level of the boundary problem solver fails to produce a solution, we should be near the boundary of the region containing solutions. We exploit the symmetry of the problem by combining results from mirror regions to obtain an improved estimate of the boundaries. Some of the red patches are possibly larger; these are indicated with a dashed line on the boundary in Fig. 3.

We have verified these results using a shooting method, as described in Appendix A2. In particular, this provides evidence that b_* is the only doubly undercompressive solution.

2. Shooting method for traveling wave solutions

We used a shooting method to verify the results from our collocation method describe above. In this vein we attempt to compute the minimum distance between the unstable manifold of the left-hand point $\mathcal{US}(-\infty)$, and the stable manifold of the right-hand point $\mathcal{S}(\infty)$ (see text), in a plane dividing the two points $P = \{(S,S',S'') : S = b_p\}$. Here b_P is a point in between b_l and b_r, typically $b_P = \frac{1}{2}(b_l + b_r)$. As in Bertozzi *et al.*,[14] we refer to P as a Poincaré section.

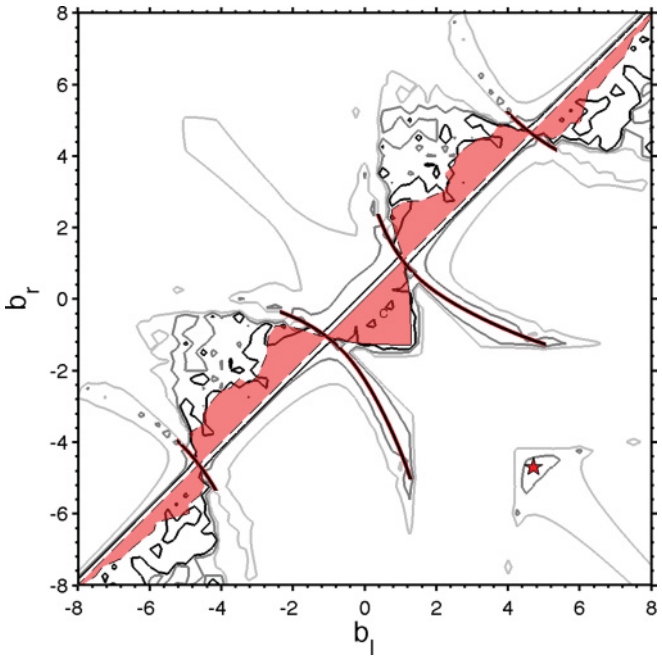

FIG. 9. (Color online) Contours of $d_{\min}$ at levels 0.01, 0.5, 5, in black, gray, and light gray lines, respectively. Red (shaded) regions are the traveling wave solutions found by collocation.

Let us define the following:

$$d^*_{\min} = \text{min. distance between } \mathcal{US}(-\infty) \cap P, \mathcal{S}(\infty) \cap P,$$
$$d_{\min} = \text{numerically estimated value of } d^*_{\min} \tag{11}$$

Note that a solution to the boundary-value problem exists when $d^*_{\min} = 0$.

To compute $d_{\min}$, we integrated (3) using an explicit ODE integrator, starting at a distance of δ ($=10^{-5}$) from $(b_{l(r)},0,0)$, on the tangent space to the unstable (stable) manifolds at these points. If the dimension of the particular invariant manifold is one, this requires two integrations. If the dimension is two, then the space of initial conditions can be parameterized with a single variable θ as $\delta(u_1 \cos\theta + u_2 \sin\theta)$, where u_1,u_2 are linearly independent, normalized vectors spanning the tangent space to the manifold at $(b_{l(r)},0,0)$, and we compute the trajectories for a finite number of evenly spaced θ values.

We keep track of where each trajectory intersects P and compute the minimum distance between the two sets of points on the Poincaré section, as well as the points which achieve, or come close to, this minimum value. We then refine the grid about these points (if at least one of the manifolds has two dimensions) and integrate the new trajectories, continuing in this manner until the minimum distance converges to some value $d_{\min}$ or is less than some tolerance level (10^{-5}).

When both manifolds are one-dimensional, this provides a robust way of measuring how "close" the two initial value problems come to each other, and hence how close we are to an actual solution of the boundary-value problem, given b_l,b_r can vary. When at least one of the manifolds is two-dimensional, this method does not necessarily converge to the true value $d^*_{\min}$; occasionally the manifold changes so rapidly with θ along the Poincaré section that it is extremely difficult find the value that comes closest to the other manifold, so that $d_{\min} > d^*_{\min}$ and in particular actual intersections, where $d^*_{\min} = 0$, may be missed. Hence, we cannot unequivocally determine existence or nonexistence with this method, but when combined with the collocation method it provides a way to gain confidence in certain claims.

We computed $d_{\min}$ on a grid with spacing 0.25. Figure 9 shows the contours of $d_{\min}$, as well as regions where we have found solutions with the collocation method. The figure shows good correlation between regions where we have found solutions (red shading, lines, and star) and regions with low $d_{\min}$ (dark contour). In particular, it appears that b_* is the only doubly undercompressive solution, as comparison with Fig. 3 shows no other local minima of $d_{\min}$ in regions where traveling waves would be doubly undercompressive.

3. Numerical method to solve PDE (2)

Our numerical method is semi-implicit in time and computes spatial derivatives based on second-order centered differences. The boundary conditions are $b(0) = b_l$, $b(L) = b_r$, $b''(0) = 0, b''(L) = 0$, where L is the length of the domain. The time increment was calculated by weighting the solution at the future time step by a factor θ and the solution at the present time step by a factor $1 - \theta$ and solving the resulting nonlinear equations using Newton's method; usually only one iteration was needed, and the results were not sensitive to θ.

The semi-implicit time step produces a stable scheme; however, the discretization creates numerical diffusion which is proportional[25] to Δt, and this changes the values of the undercompressive shocks. Therefore we chose Δt small to control numerical diffusion.

[1]G. Whitesides and B. Grzybowski, Science **295**, 2418 (2002).
[2]P. Sigmund, Phys. Rev. **184**, 383 (1969); J. Mater. Sci. **8**, 1545 (1973).
[3]R. M. Bradley and J. M. E. Harper, J. Vac. Sci. Technol. A **6**, 2390 (1988).
[4]W. L. Chan and E. Chason, J. Appl. Phys. **101**, 121301 (2007).
[5]M. J. Vasile, Z. Niu, R. Nassar, W. Zhang, and S. Liu, J. Vac. Sci. Technol. B **15**, 2350 (1997).
[6]D. Adams, M. Vasile, T. Mayer, and V. Hodges, J. Vac. Sci. Technol. B **21**, 2334 (2003).
[7]J. Li, D. Stein, C. McMullan, D. Branton, M. J. Aziz, and J. A. Golovchenko, Nature (London) **412**, 166 (2001).
[8]D. Stein, J. Li, and J. A. Golovchenko, Phys. Rev. Lett. **89**, 276106 (2002).
[9]S. Facsko, T. Dekorsy, C. Koerdt, C. Trappe, H. Kurz, A. Vogt, and H. Hartnagel, Science **285**, 1551 (1999).
[10]F. Frost, A. Schindler, and F. Bigl, Phys. Rev. Lett. **85**, 4116 (2000).
[11]A. Cuenat, H. B. George, K.-C. Chang, J. Blakely, and M. J. Aziz, Adv. Mater. **17**, 2845 (2005).

[12]H. Chen, O. Urquidez, S. Ichim, L. Rodriguez, M. Brenner, and M. Aziz, Science **310**, 294 (2005).
[13]G. B. Whitham, *Linear and Nonlinear Waves*, Pure and Applied Mathematics (Wiley, New York, 1974).
[14]A. L. Bertozzi, A. Munch, and M. Shearer, Physica D **134**, 431 (1999).
[15]A. Bertozzi and M. Shearer, SIAM J. Math. Anal. **32**, 194 (2000).
[16]C. S. Madi *et al*., Phys. Rev. Lett. **106**, 066101 (2011).
[17]Y. Yamamura, Y. Itikawa, and N. Itoh, "Angular dependence of sputtering yields of monatomic solids," Report No. IPPJ-AM-26 (unpublished).
[18]S. Norris *et al*., Nature Comm. **2**, 276 (2011).
[19]C. S. Madi, B. Davidovitch, H. B. George, S. A. Norris, M. P. Brenner, and M. J. Aziz, Phys. Rev. Lett. **101**, 246102 (2008).
[20]N. Kalyanasundaram, J. Freund, and H. T. Johnson, Appl. Phys. Lett. **92**, 131909 (2008).
[21]M. Hossain, K. Das, J. Freund, and H. Johnson, Appl. Phys. Lett. **99**, 151913 (2011).
[22]H. Chen, Ph.D. thesis, Harvard University, 2005.
[23]L. Shampine, M. Reichelt, and J. Kierzenka, "Solving boundary value problems for ordinary differential equations in MATLAB with bvp4c," [http://www.mathworks.com/bvp_tutorial].
[24]W. H. Press, *Numerical Recipes: The Art of Scientific Computing*, 3rd ed. (Cambridge University Press, Cambridge, 2007).
[25]J. Goodman and A. Majda, J. Comput. Phys. **58**, 336 (1985).